

Supporting Information

Phase field modelling of crystal growth of NaCl in two dimensions

Chao Dun Tan and Georg Hähner

A. Derivation of the characteristic time parameter, τ

The Allen-Cahn equation that describes the temporal evolution of the phase parameter, ϕ , is

$$\frac{1}{L} \frac{\partial \phi}{\partial t} = G \nabla^2 \phi + \omega (1 - \phi^2)(\phi - \lambda c) - G \kappa |\nabla \phi|, \quad (\text{A.1})$$

where L is the interface mobility in units of $\text{m}^3 \text{J}^{-1} \text{s}^{-1}$, G is the gradient energy coefficient in units of J m^{-1} and ω is the double-well barrier height in energy density units (J m^{-3}).¹⁻³ It is common practice in the literature³⁻⁵ to normalize equation (A.1) with ω , leading to the precipitation equation derived by Xu and Meakin (2008):⁶⁻⁸

$$\tau \frac{\partial \phi}{\partial t} = \varepsilon^2 \nabla^2 \phi + (1 - \phi^2)(\phi - \lambda c) - \varepsilon^2 \kappa |\nabla \phi|, \quad (\text{A.2})$$

where $\tau = 1/(L\omega)$ and $\varepsilon = \sqrt{G/\omega}$.

The double-well barrier height can be related to both the interfacial energy, S , and the interface width parameter, ε :^{1, 9, 10}

$$S = \omega \varepsilon^2 \int_{-\infty}^{+\infty} \left(\frac{d}{dr} \phi_0(r) \right)^2 dr = \frac{2\sqrt{2}}{3} \omega \varepsilon, \quad (\text{A.3})$$

where $\phi_0(r)$ is the equilibrium profile of ϕ centred at the interface, which takes the form of a hyperbolic tangent:

$$\phi_0(r) = \tanh\left(\frac{r}{\sqrt{2}\varepsilon}\right). \quad (\text{A.4})$$

Rearranging eq. (A.3) for ω leads to eq. (2.4) in the main text:

$$\tau = \frac{1}{L\omega} = \frac{2\sqrt{2}\varepsilon}{3LS}.$$

B. Numerical determination of the stable ϕ profile

Fig B (left) below shows the ratio W/ε of the fitted and designated width parameter, W and ε , respectively, for an input of $\varepsilon=500$ nm and $\Delta t = 5$ μs . At the start of the numerical determination procedure, the ratio is small due to the 'sharp' initial profile, but soon converges to 1, indicating $W = \varepsilon$ and a stable hyperbolic profile is achieved. Fig B (right) shows how the initially 'sharp' profile broadens and converges to the stable hyperbolic tangent profile for increasing iteration numbers, N_{It} .

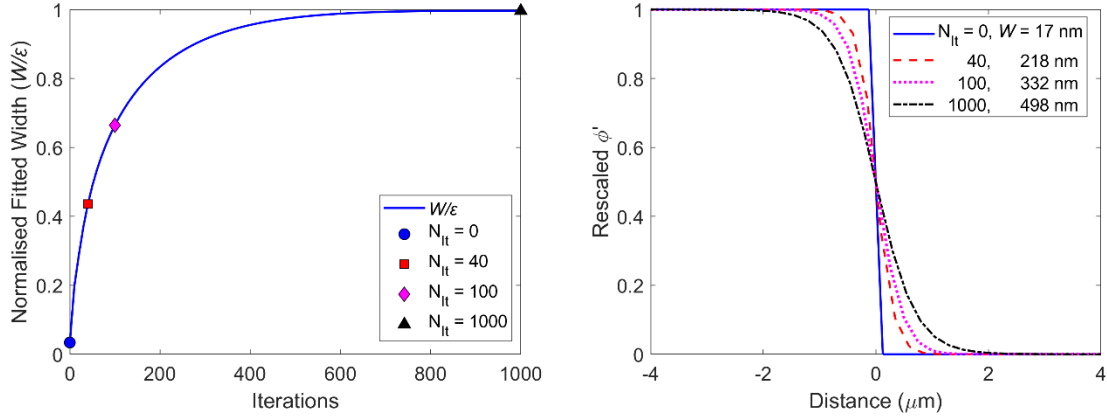


Fig B: On the left the ratio between the fitted and designated width parameter, W/ε , against the number of iterations is shown. The set ε was 500 nm. On the right the scaled ϕ' profile for different N_{It} (indicated by the markers in the left figure) is displayed.

C. 'Sharp' and diffuse concentration profiles

Fig C below shows the scaled phase, ϕ' , and concentration profiles, c , at $t = 0$ s (left) and $t=0.1$ s (right) for $\varepsilon = 500$ nm and $c_\infty = 0.27$ ($\Omega = 1.3$). The shape of the ϕ' profile does not change while the interface position (R at $\phi' = 0.5$) has moved just 0.2 μm after 0.1 s (corresponding to 4000 iterations). In contrast, the 'sharp' concentration profile (Fig. C, left) changes drastically during the same period and evolves into the diffusion profile shown in Fig. C, right.

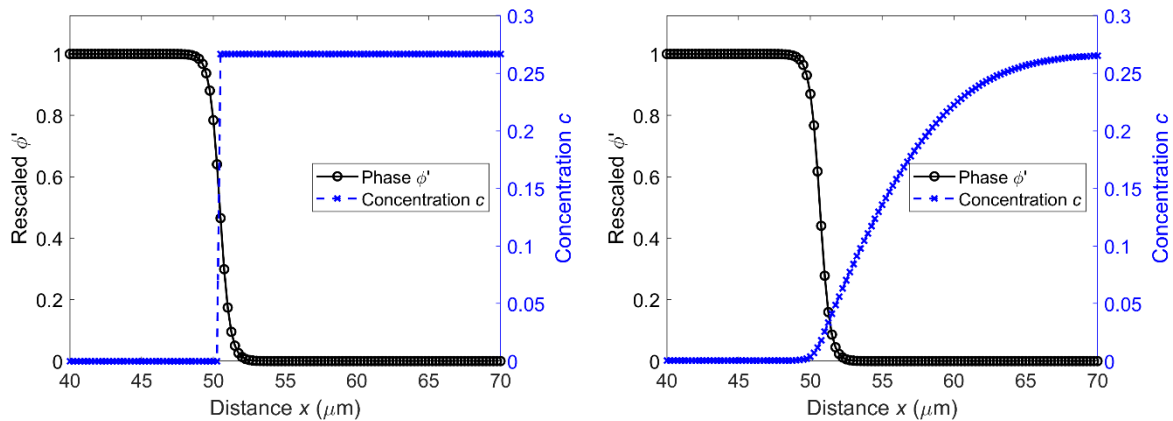


Fig C: ϕ' and c profiles at the start of the simulation (left) and after 4000 iterations (right), corresponding to $t = 0.1$ s, for $\varepsilon = 500$ nm and $c_\infty = 0.27$ ($\Omega = 1.3$).

D. Isotropic crystal growth of circular seeds

Isotropic crystal growth was simulated using $\Omega = 2.0$ (equivalent to $c_\infty = 0.82$) for up to 2 s using circular seeds of different initial radii, R_0 , to investigate how the growth speed depends on curvature. Similar to the planar growth simulations and simulations with fourfold symmetry, the initial phase profile was determined numerically and the concentration profile was a 'sharp' profile. The initial radii tested were 30, 40, 50 and 60 μm .

Fig D1 below shows an example of the simulated isotropic crystal growth for $R_0 = 30 \mu\text{m}$ after 2 s.

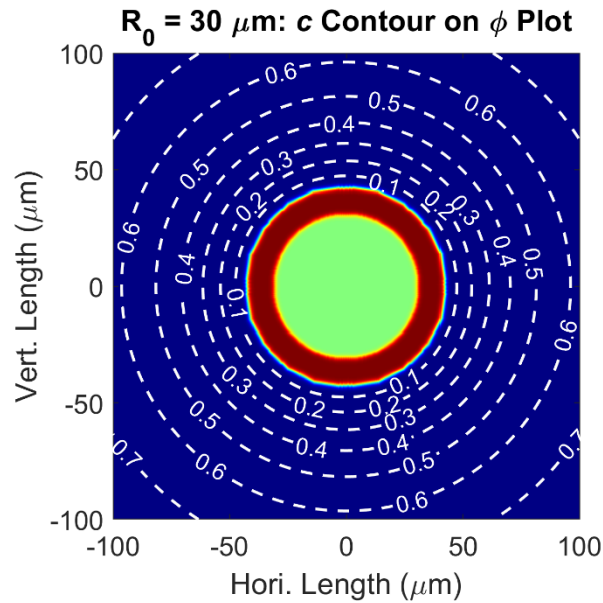


Fig D1: Initial (light green) and final shape (red) for isotropic crystal growth, for a circular seed with radius $R_0 = 30 \mu\text{m}$. The contour lines indicate the concentration, c .

Fig D2 shows $\Delta R = R(t) - R_0$ (left) and $\zeta_{1/2}(t)$ (right) against time for different values of R_0 . The radius $R(t)$ was obtained from the overall area of the circular crystal, i.e., $R(t) = \sqrt{\text{Area}(t)/\pi}$. $\zeta_{1/2}(t)$ was determined using the phase and concentration profiles extracted along different directions of the circular crystal during the simulations.

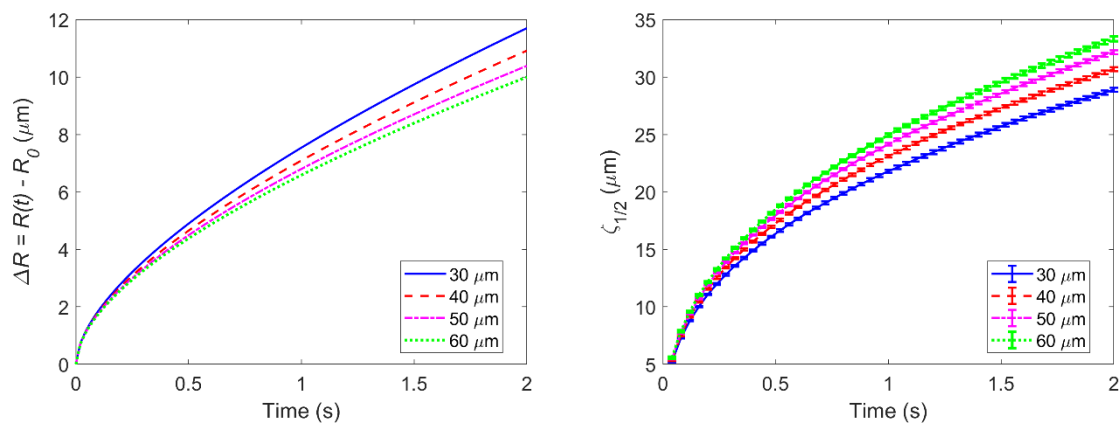


Fig D2: The difference in the time-dependent radius and the initial radius, $R(t) - R_0$, (left) and the diffusive length $\zeta_{1/2}$ with error bars (right) against time.

$\zeta_{1/2}$ was established by first determining the distance from the origin of the simulation domain to the point where $c = c_\infty/2$ (via linear interpolation), followed by subtracting the distance of the solid-liquid interface (obtained from fitting the ϕ profile). A sketch depicting $\zeta_{1/2}$ is shown in Fig D3.

For each simulation, the average and standard deviation of $\zeta_{1/2}$ were evaluated from 19 pairs of ϕ and c profiles. The maximum deviations of $\zeta_{1/2}$ for all simulations is not higher than 1.5% as displayed by the error bars in Fig D2 (right). This means that the concentration distributions around the circular crystals are fairly homogeneous during the simulations and the uncertainties in growth speeds evaluated from eq. (3.4) using these mean values of $\zeta_{1/2}$ will be relatively small.

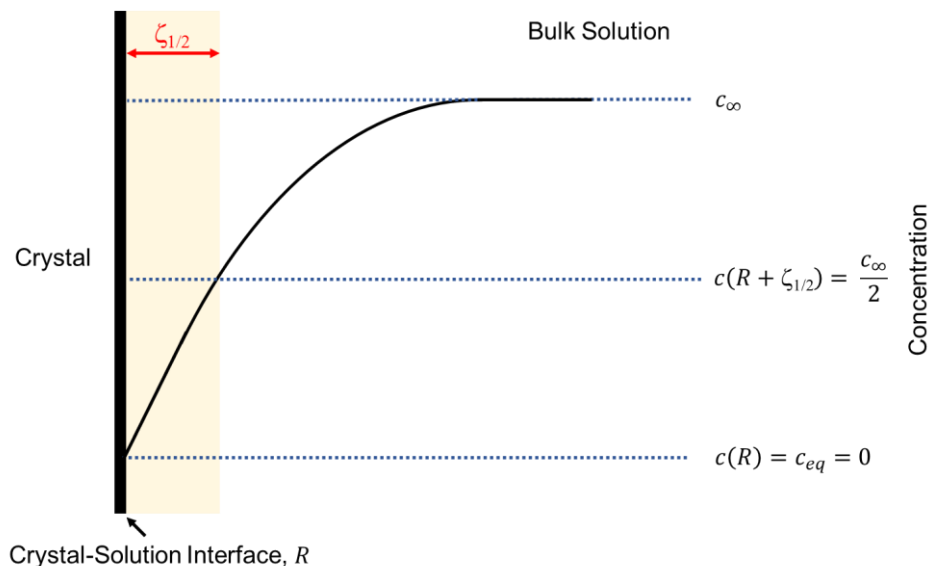


Fig D3: Sketch of the concentration profile indicating $c = c_{\infty}/2$ and the resulting diffusive length $\zeta_{1/2}$.

Fig D4 (left) shows the instantaneous growth speeds, dR/dt , against time obtained from PF simulations, $\check{v}_{sim}(t)$ (solid lines), for different initial radii R_0 . Also plotted are the growth speeds determined with the analytical expression for $\check{v}_{2D}(t)$ (eq. 3.4) from the steady-state model. The ratios of the simulated and analytical growth speeds, $\check{v}_{sim}/\check{v}_{2D}$, are plotted in Fig D4 (right).

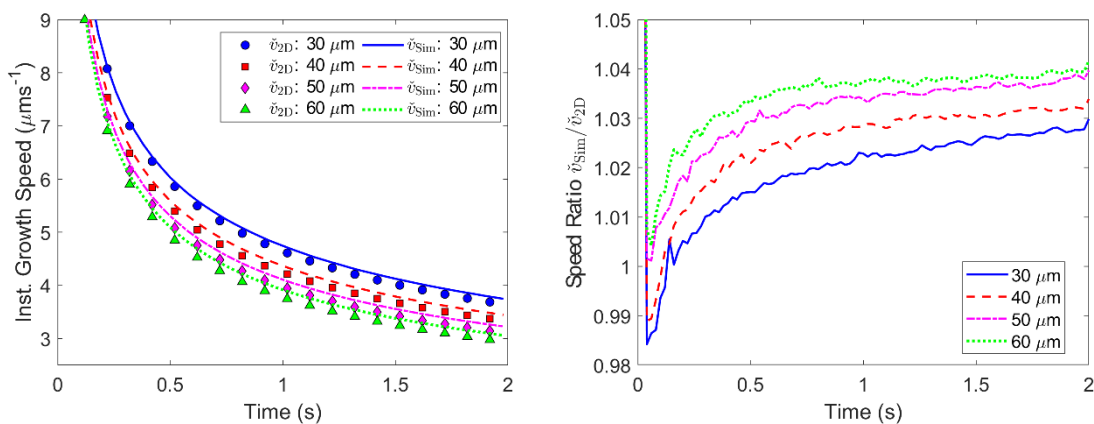


Fig D4: Simulated (solid lines) and analytical instantaneous growth speeds (markers), \check{v}_{sim} and \check{v}_{2D} , (left), and their ratios, $\check{v}_{sim}/\check{v}_{2D}$, (right) for different values of R_0 against time.

After the initial period when the concentration profiles have evolved from the ‘sharp’ profiles, the analytical growth speed for $R_0=60\ \mu\text{m}$ shows the biggest deviation from its simulated counterpart, with a maximum percentage difference of $\sim 4\%$ (shown on Fig D4 right). For smaller R_0 values, the deviations are lower.

With deviations of not more than 5%, the simulated growth speeds are in good agreement with those obtained from the steady-state approximation. Hence, we conclude that non-physical contributions that can arise from the curvature of the diffuse ϕ interface are not significant, and curvature dependent growth is described reasonably well by the PF model.

E. Simulations with circular seeds and fourfold symmetry

When a spherical/circular seed is used, the circle approximated by the grid is not perfect due to the discretization of the simulation grid. Fig E shows the initial shape of a circular seed (light green) and its final shape (red) after 7s simulated for anisotropy offset angles of $\theta_0 = 37^\circ$ (left) and 71° (right), respectively, using $\varepsilon = 700\ \text{nm}$ and $\Omega = 2.4$. The grid cell of the circular seed that develops into a vertex depends on the initial radius of the (non-ideal) circular shape, R_0 , the width, ε , and the angle, θ_0 , leading to some variation in the appearance of the overall final crystal. Note that the overall areas of the final crystals are essentially identical and both have four-fold *rotational* symmetry. To ensure the crystals have both rotational as well as mirror plane symmetry, i.e., are much less dependent on the combination of R_0 , ε , and θ_0 , we used small protrusions on the seeds. The crystal is then much less prone to develop four-fold rotational but no mirror symmetry. However, depending on the specific conditions used small deviations from mirror symmetry can still develop.

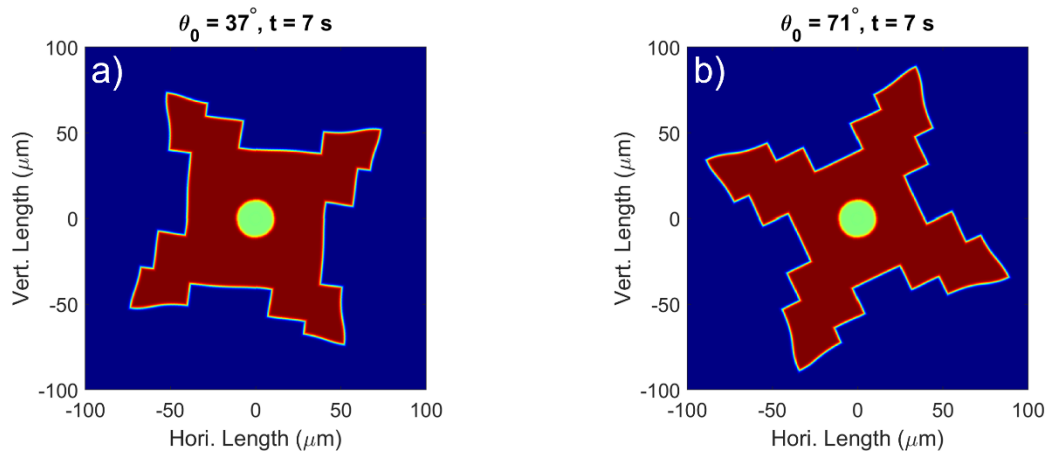


Fig E: Initial (light green) and final (red) crystal shapes after 7s using a circular seed with $R_0 = 10\ \mu\text{m}$, $\varepsilon = 700\ \text{nm}$, $\Omega = 2.4$, for $\theta_0 = 37^\circ$ (left) and $\theta_0 = 71^\circ$ (right).

F. Simulation in a quadrant

Since both the crystal structure of NaCl and the simulation grid possess fourfold symmetry, the simulations were performed in a quadrant of the overall area of interest only^{4,7} to reduce computational time. For the outer boundaries of the overall area, no-flux Neumann conditions were used. During the simulations, symmetry was preserved by treating the values along the x-axis as boundary values for the y-axis and vice versa when the spatial derivatives at the inner boundaries were evaluated.

Fig. F below shows the entire simulation domain for areas of $480 \times 480 \mu\text{m}^2$ (left) and $800 \times 800 \mu\text{m}^2$ (right), respectively, and two different concentration values together with the initial seeds and the resulting final crystals.

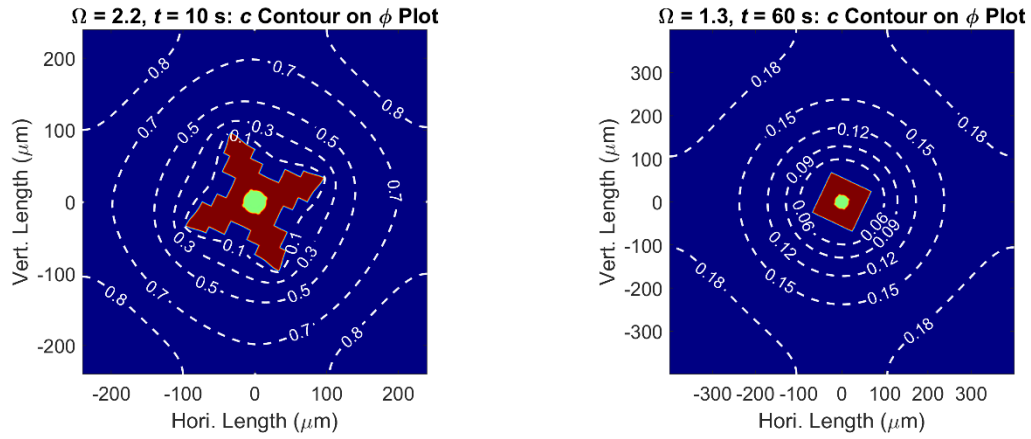


Fig F: Entire simulation domain and final crystal shapes (red) for a circular seed (light green) of radius $R_0=15 \mu\text{m}$ with protrusions, for (left) $\Omega = 2.2$ ($c_\infty = 0.97$), $\varepsilon = 700 \text{ nm}$, and $\theta_0 = 19^\circ$ after 10 s, and (right) for $\Omega = 1.3$ ($c_\infty = 0.26$), $\varepsilon = 1 \mu\text{m}$ and $\theta_0 = 19^\circ$ after 60 s. Simulations were run for finite reservoirs with no-flux Neumann boundary conditions.

G. Concentration after 10 s for $\Omega = 2.2$

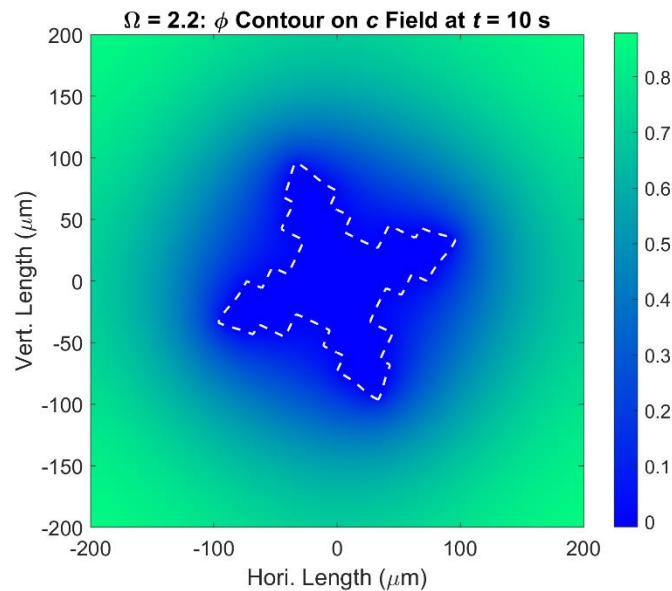


Fig. G: Concentration distribution for the NaCl solid shown in Fig. F, left. The solid is indicated by the white dashed line. There is a depletion of ions in the areas between the 'branches' of the solid. Because of the boundary conditions used (finite reservoir as in experiments with microchannels) the growth speed slows down faster than in an 'infinite reservoir' and even after longer periods the non-compact structure will in general not grow

into a fully compact structure. If non-compact growth is followed by compact growth at a later stage this will often result in a hybrid shape as has been observed in experiments, e.g.,¹¹⁻¹³.

1. R. S. Qin and H. K. Bhadeshia, *Mater. Sci. Technol.*, 2010, **26**, 803-811.
2. S. Yang, N. Ukrainczyk, A. Caggiano and E. Koenders, *Appl. Sci.-Basel*, 2021, **11**, 2464.
3. N. Moelans, B. Blanpain and P. Wollants, *Calphad*, 2008, **32**, 268-294.
4. A. Karma and W.-J. Rappel, *Phys. Rev. E*, 1998, **57**, 4323-4349.
5. R. Kobayashi, *Physica D*, 1993, **63**, 410-423.
6. Z. J. Xu and P. Meakin, *J. Chem. Phys.*, 2008, **129**, 014705.
7. Z. J. Xu and P. Meakin, *J. Chem. Phys.*, 2011, **134**, 044137.
8. Z. Xu, H. Huang, X. Li and P. Meakin, *Comput. Phys. Commun.*, 2012, **183**, 15-19.
9. S. M. Allen and J. W. Cahn, *Acta Metallurgica*, 1979, **27**, 1085-1095.
10. A. A. Wheeler, *J. Stat. Phys.*, 1999, **95**, 1245-1280.
11. A. Naillon, P. Duru, M. Marcoux and M. Prat, *J. Cryst. Growth*, 2015, **422**, 52-61.
12. A. Naillon, P. Joseph and M. Prat, *J. Cryst. Growth*, 2017, **463**, 201-210.
13. J. Desarnaud, H. Derluyn, J. Carmeliet, D. Bonn and N. Shahidzadeh, *J. Phys. Chem. Lett.*, 2018, **9**, 2961-2966.